



UNIVERSITY OF LEEDS

This is a repository copy of *Depth-varying seismogenesis on an oceanic detachment fault at 13°20'N on the Mid-Atlantic Ridge*.

White Rose Research Online URL for this paper:
<http://eprints.whiterose.ac.uk/121064/>

Version: Accepted Version

Article:

Craig, TJ orcid.org/0000-0003-2198-9172 and Parnell-Turner, R (2017) Depth-varying seismogenesis on an oceanic detachment fault at 13°20'N on the Mid-Atlantic Ridge. *Earth and Planetary Science Letters*, 479. pp. 60-70. ISSN 0012-821X

<https://doi.org/10.1016/j.epsl.2017.09.020>

(c) 2017, Elsevier B.V. This manuscript version is made available under the CC BY-NC-ND 4.0 license <https://creativecommons.org/licenses/by-nc-nd/4.0/>

Reuse

Items deposited in White Rose Research Online are protected by copyright, with all rights reserved unless indicated otherwise. They may be downloaded and/or printed for private study, or other acts as permitted by national copyright laws. The publisher or other rights holders may allow further reproduction and re-use of the full text version. This is indicated by the licence information on the White Rose Research Online record for the item.

Takedown

If you consider content in White Rose Research Online to be in breach of UK law, please notify us by emailing eprints@whiterose.ac.uk including the URL of the record and the reason for the withdrawal request.



eprints@whiterose.ac.uk
<https://eprints.whiterose.ac.uk/>

Depth-varying seismogenesis on an oceanic detachment fault at 13°20'N on the Mid-Atlantic Ridge

Timothy J. Craig^{1,*}, Ross Parnell-Turner²

¹ Institute of Geophysics and Tectonics,
School of Earth and Environment, University of Leeds,
Leeds, LS2 9JT, UK.

² Department of Geology and Geophysics,
Woods Hole Oceanographic Institution,
Woods Hole Road, Woods Hole, MA 02543, USA.

*Corresponding author: t.j.craig[at]leeds.ac.uk

August 31, 2017

Abstract

1
2 Extension at slow- and intermediate-spreading mid-ocean ridges
3 is commonly accommodated through slip on long-lived faults called
4 oceanic detachments. These curved, convex-upward faults consist of
5 a steeply-dipping section thought to be rooted in the lower crust or
6 upper mantle which rotates to progressively shallower dip-angles at
7 shallower depths. The commonly-observed result is a domed, sub-
8 horizontal oceanic core complex at the seabed. Although it is ac-
9 cepted that detachment faults can accumulate kilometre-scale off-
10 sets over millions of years, the mechanism of slip, and their capac-
11 ity to sustain the shear stresses necessary to produce large earth-
12 quakes, remains debated. Here we present a comprehensive seismo-
13 logical study of an active oceanic detachment fault system on the
14 Mid-Atlantic Ridge near 13°20'N, combining the results from a local
15 ocean-bottom seismograph deployment with waveform inversion of a
16 series of larger teleseismically-observed earthquakes. The unique co-
17 incidence of these two datasets provides a comprehensive definition of
18 rupture on the fault, from the uppermost mantle to the seabed. Our

19 results demonstrate that although slip on the deep, steeply-dipping
20 portion of detachment faults is accommodated by failure in numer-
21 ous microearthquakes, the shallow, gently-dipping section of the fault
22 within the upper few kilometres is relatively strong, and is capable of
23 producing large-magnitude earthquakes. This result brings into ques-
24 tion the current paradigm that the shallow sections of oceanic detach-
25 ment faults are dominated by low-friction mineralogies and therefore
26 slip aseismically, but is consistent with observations from continen-
27 tal detachment faults. Slip on the shallow portion of active detach-
28 ment faults at relatively low angles may therefore account for many
29 more large-magnitude earthquakes at mid-ocean ridges than previ-
30 ously thought, and suggests that the lithospheric strength at slow-
31 spreading mid-ocean ridges may be concentrated at shallow depths.
32

33 1 Introduction

34 Earthquake activity at mid-ocean ridges provides an insight into the thermal
35 and rheological state of the lithosphere as it is created and subsequently
36 deformed (e.g. Sykes, 1967). At slow-spreading ridges, a significant portion
37 of plate separation may be accommodated by slip on long-lived detachment
38 faults, which are thought to initiate at steep dips and then roll over to become
39 sub-horizontal at the seafloor (Cann et al., 1997; Morris et al., 2009). This
40 process leads to the exhumation of lower crustal and upper mantle rocks
41 at the seabed, which often form kilometre-scale domes called oceanic core
42 complexes (OCCs; Tucholke et al., 1998; MacLeod et al., 2002; Dick et al.,
43 2008; Escartin and Canales, 2011).

44 While seafloor mapping and sampling, and active-source seismic imaging
45 provide a static picture of these features (e.g. Dick, 1989; Cann et al., 1997;
46 Blackman et al., 2009), the subsurface mechanics of the process of roll-over
47 remains enigmatic. Short-duration local ocean bottom seismograph (OBS)
48 experiments have shown that microearthquakes in these settings consistently
49 occur at depths between 3 and 7 km below seafloor (bsf; Toomey et al.,
50 1985; Kong et al., 1992; Wolfe et al., 1995; Grevemeyer et al., 2013). Some
51 of these earlier studies lacked the high-resolution bathymetry necessary to
52 identify detachment faults prior to deployment, and hence used networks

53 not optimised for studying earthquakes associated with these faults. Two
54 deployments of densely-spaced OBS networks specifically targeting identi-
55 fied active core complexes in the North Atlantic Ocean have shown that the
56 pattern of microearthquakes defines a steep-dipping planar normal fault sur-
57 face at depth. However rupture at depths shallower than 4 km bsf remains
58 undetected (deMartin et al., 2007; Parnell-Turner et al., 2017). This appar-
59 ent lack of shallow seismicity has been suggested to be the result of fractured,
60 permeable crust being incapable of supporting sufficient stresses to produce
61 earthquakes, or the presence of hydrothermally-altered fault gouge material
62 leading to aseismic slip (deMartin et al., 2007; Grevemeyer et al., 2013). In
63 contrast, continental detachment faults associated with metamorphic core
64 complexes, for example in Papua New Guinea, may be capable of hosting
65 large-magnitude, shallowly-dipping normal faulting earthquakes on their up-
66 permost sections (Abers, 1991; Abers et al., 1997), although recent geodetic
67 work instead suggests much of the slip may be accommodated aseismically
68 (Wallace et al., 2014).

69 A large proportion of the slow-spreading Mid-Atlantic Ridge (MAR)
70 shows evidence for detachment faulting and the accretion of oceanic crust
71 through OCC formation (Smith et al., 2006; Escartín et al., 2008). Studies
72 of teleseismically-detected earthquakes at slow-spreading ridges have shown
73 that events in the median valley have typical focal depths of 1–4 km bsf,
74 and dip angles of $\sim 45^\circ$ (Huang et al., 1986), consistent with global sur-
75 veys of large earthquakes at other slow-spreading ridges (Jemsek et al., 1986;
76 Solomon and Huang, 1987). Lacking the constraints necessary to relate these
77 earthquakes to a particular fault, they have been assumed to be related to
78 planar rift-border faults, and not to be associated with detachment fault-
79 ing. This assumption, however, contrasts with evidence that detachment-
80 dominated segments of the Mid-Atlantic Ridge generate more earthquakes
81 in both teleseismic and hydroacoustic catalogues (Escartín et al., 2008; Olive
82 and Escartín, 2016), suggesting a link between the presence of detachment
83 faulting and the production of large mid-ocean ridge earthquakes.

84 Hence, three apparently disparate modes of detachment fault behavior
85 have been identified seismologically. First, dominantly aseismic, uncoupled

86 behaviour is expected for oceanic detachments associated with weak, low
87 friction mineralogies; second, high-moment-release, teleseismically-detected
88 earthquakes are observed along sections of detachment-fault dominated mid-
89 ocean ridge segments; and third, large-magnitude earthquakes are associated
90 with detachment faulting bounding metamorphic core complexes on the con-
91 tinents. In an attempt to characterise the full seismogenic behaviour of a
92 detachment fault across the complete range of observational scales, we con-
93 sider the seismicity associated with an actively slipping oceanic detachment
94 fault on the MAR near $13^{\circ}20'N$, integrating the results from a local OBS de-
95 ployment with observations of co-located large earthquakes from the global
96 seismic network.

97 **2 Seismicity near the $13^{\circ}20'N$ detachment**

98 We focus on the area near $13^{\circ}20'N$ on the MAR, where an active OCC
99 has been previously extensively surveyed and sampled (Smith et al., 2006;
100 MacLeod et al., 2009; Mallows and Searle, 2012; Escartín et al., 2017; Bon-
101 nemains et al., 2017). The exposed fault surface has prominent spreading-
102 parallel corrugations, and is thought to record ~ 9 km of heave since its
103 initiation at ~ 0.4 Ma (MacLeod et al., 2009; Mallows and Searle, 2012).

104 In 2014, an array of 25 OBSs detected $\sim 240,000$ microearthquakes near
105 the $13^{\circ}20'N$ detachment fault over a period of six months (Parnell-Turner
106 et al., 2017). There are two domains of seismicity: reverse-faulting earth-
107 quakes beneath the dome at 3–7 km bsf, attributed to internal compres-
108 sion within the bending footwall; and normal-faulting earthquakes towards
109 the centre of the axial valley, at depths of 5–12 km bsf (Figure 1 and his-
110 tograms on Figures 4a and 5). The along-axis pattern of normal-faulting
111 microearthquakes suggests that at depth, the active detachment fault ex-
112 tends beyond the limits of the exposed corrugated surface. These normal
113 faulting earthquakes have a composite focal mechanism indicating slip on a
114 steeply eastward-dipping plane (see Supplementary Table 1), interpreted to
115 be the downdip portion of the detachment fault in the region where a coherent
116 fault zone forms. The depth extent and apparent dip of normal-faulting mi-

117 croearthquakes is consistent with that observed at the active Trans-Atlantic
118 Geotraverse (TAG) detachment near 26°N on the MAR (deMartin et al.,
119 2007). The lack of shallow microearthquakes at these two locations means
120 that the style of deformation (e.g., aseismic slip, or seismic failure in large
121 or small earthquakes) on the shallow, roll-over portion of detachment faults
122 remains uncertain.

123 Over the last decade, three large-magnitude, teleseismically-detected normal-
124 faulting earthquakes have occurred in the vicinity of the 13°20'N OCC. A
125 M_w 5.7 event that occurred on the 7th December 2008 (hereafter referred to
126 as the 2008 mainshock) was followed a day later by a M_w 5.5 aftershock, and
127 a third event, M_w 5.7, occurred on 20th October 2016. The ability to relate a
128 given earthquake with a specific fault near the mid-ocean ridge is hampered
129 by the uncertainty in earthquake location and the absence of near-field data.
130 In order to overcome this limitation, we seek to determine the most likely
131 hypocentral location for these three events, and therefore their relationship
132 to the local tectonic structures, by evaluating five possible scenarios. First,
133 that slip occurred on the shallow portion of the 13°20'N detachment which
134 lacks microearthquakes; second, that these events are co-located with mi-
135 croearthquakes on the steeper, deeper detachment surface; third, that these
136 events are shallow antithetic events within the 13°20'N detachment footwall
137 block; fourth, that they represent breakup of the detachment hanging wall in
138 the formation of rider blocks; or fifth, that they are unrelated to the 13°20'N
139 detachment fault and occurred on another fault nearby.

140 **3 Constraints on earthquake location**

141 Earthquake locations based on globally-observed travel times for these earth-
142 quakes indicate that they all occurred within 10 km of the active 13°20'N
143 detachment (Figure 1, Table S2; International Seismological Centre 2014). In
144 particular, the 2016 event co-locates with the 13°20'N detachment, slightly
145 up-dip of the observed microseismicity. Quoted catalogue uncertainties sug-
146 gest that these locations are accurate to $\sim \pm 10$ km [National Earthquake
147 Information Center; NEIC], comparable to the mean error in global seis-

148 mological hypocentre locations, based on geodetic calibration (Lohman and
149 Simons, 2005; Weston et al., 2012). Independently calculated locations for
150 these earthquakes from different agencies show a strong clustering within
151 this level of uncertainty (see Figure 1 and Table S1). Although absolute
152 locations for these earthquakes are limited by the lack of any near-source
153 data, improved data coverage between 2008 and 2016 suggests that the 2016
154 location is probably more reliable. Despite these improvements, attributing
155 these events to specific tectonic structures, and relating them to one another,
156 remains difficult.

157 We relocate the three teleseismically-observed earthquakes relative to one
158 another using inter-event times determined using waveform cross-correlation
159 (see Figure 3). This approach refines inter-event distances, although it
160 does not provide absolute locations relative to geographic features (such as
161 the 13°20'N OCC). Exploiting the broad-scale similarity in mechanism and
162 source duration between the three teleseismically-observed earthquakes (see
163 Section 4), we relocate them relative to each other on the basis of relative
164 travel times derived from cross-correlation of the *P* and *S* waves. We use
165 a correlation window of 45 s, starting 5 s before the predicted phase arrival
166 time. Relative travel times are computed using all three components (vertical
167 for the *P* wave, east and north for the *S* wave). We initially use all stations
168 that cover the observation periods for at least two of the three events con-
169 sidered, and then limit the dataset based on the ability to visually identify
170 arrivals in the waveforms, and on the magnitude of the computed cross cor-
171 relation coefficient, using a threshold value of 0.5. Figure S1 shows the full
172 station set used for *P* and *S* waves, overlain on the radiation pattern for the
173 2016 earthquake (those for 2008 are similar). Note that station coverage is
174 not the same for all three earthquakes, leading to varying sets of station pairs
175 for the three event-pairs possible. Whilst the majority of stations active in
176 2008 cover both of the earthquakes in this year, the smaller magnitude of
177 the 8th December 2008 event leads to a smaller number of stations with clear
178 arrivals for both events.

179 We use a tapered frequency band, optimised between 0.05 and 1 Hz, for
180 the cross correlation. Expanding this band to incorporate higher frequencies

181 initially leads to a similar location offset, but the inter-event coherence, par-
182 ticularly to the 2008 aftershock, decays rapidly above 1 Hz (demonstrated in
183 Figure 3), leading to a decrease in the number of reliable inter-event travel
184 times. For the final set of relocations presented in Figure 2, we use 309 *P*-
185 wave event-pairs, and 269 *S*-wave pairs, with average cross-correlation coeffi-
186 cients of 0.75 and 0.85, respectively. Prior to relocation, the mean inter-event
187 travel-time residual is 1.02 s. After relocation, the residual decreases to 0.34
188 s (residual populations are shown on Figure 2b,c).

189 We test the relocation results by limiting the dataset to those those sta-
190 tions at epicentral distances of $<30^\circ$ (32 *P*-wave and 22 *S*-wave pairs) which
191 should be more sensitive to lateral offsets in location. This refinement leads
192 to a similar set of relocations, where the 2008 mainshock and the 2016 event
193 occur within one rupture length of each other (~ 6 km; see below). The 2008
194 aftershock is offset to the north and west, although there is some difference
195 in the magnitude of the shift for this event (Figure 2). Similarly, reloca-
196 tions using datasets limited to *P*-wave and *S*-wave arrivals alone (Figure 2a)
197 produces the same overall pattern across the three earthquakes, with the
198 main variation in the distance, but not direction, of the offset to the 2008
199 aftershock.

200 Although hampered by scant near-source data (nearest stations $>14^\circ$ epi-
201 central distance), the relocations conclusively indicate that the 2008 main-
202 shock and 2016 event (earthquakes of similar magnitude) occurred near to
203 one another. Plate spreading rates in this area are unlikely to be sufficient
204 to accumulate enough strain to produce a M_w 5.7 earthquake in the 8-year
205 inter-event period, leading us to suggest that these two earthquakes likely
206 occurred on adjoining segments of the same fault, rather than repeated rup-
207 ture of the same fault patch. The causative feature must therefore be large
208 enough to sustain a combined moment release equal to a single M_w 5.9 event.

209 In contrast to the absolute catalogue locations, the smaller 2008 after-
210 shock appears to locate to the northwest, rather than northeast, of the other
211 two events considered, although the degree of the westward shift is poorly
212 constrained (see Figure 2).

213 A northwards offset for the 2008 aftershock is common to both the relative

214 and absolute relocations, whereas the direction of the east-west offset changes
215 using the two different techniques. Precise onset times of the direct P -wave
216 are difficult to determine from the waveforms visually, particularly for the
217 lower-amplitude P -wave arrivals from the smaller 2008 mainshock, where the
218 onset amplitude is often within the level of the background noise. As a result,
219 the absolute location for this smaller event is less well constrained than for
220 the larger, and hence better resolved earthquakes. We therefore rely on the
221 absolute locations for the 2008 mainshock and 2016 event, and suggest that
222 the 2008 aftershock is somewhere to the north, although its precise location
223 is poorly determined. Any potential causative relationship between the two
224 earthquakes in 2008 is unknown, but if the mechanism relating these two
225 events is assumed to be static stress transfer, then the east-west offset of
226 the aftershock relative to the 2008 mainshock is likely to be less than the
227 northwards offset.

228 In the frequency band used for relocation, similarity in overall mechanism
229 and locations of the three earthquakes allow their relative times to be deter-
230 mined. At higher frequencies (> 1 Hz), similarity between the waveforms for
231 the two larger events remains apparent, indicating their proximity to one an-
232 other and similar influence of near-source effects on the waveform. Waveforms
233 for the 2008 aftershock, while similar to the other events at low frequencies,
234 are notably different at higher frequencies, indicating a marginally different
235 rupture process and near-source scattering effects (Figure 3).

236 4 Source mechanisms and fault geometry

237 To supplement the relative and absolute constraints on the earthquake loca-
238 tions, we use teleseismic waveform inversion to constrain the source mecha-
239 nism, rupture duration and depth for these three earthquakes using P - and
240 SH -waves, treating each earthquake as a finite-duration point-source cen-
241 troid.

242 We invert long-period waveforms observed at teleseismic distances (30° -
243 80° epicentral distance) to determine earthquake mechanism parameters, cen-
244 troid depth, moment, and source duration, using the approach of Zwick et al.

245 (1994). Our method follows that previously used for mid-ocean ridge earth-
246 quakes (Huang et al., 1986; Jemsek et al., 1986; Huang and Solomon, 1987),
247 and for the determination of earthquake source parameters in other oceanic
248 settings (Abers, 1991; Abers et al., 1997; Tilmann et al., 2010; Craig et al.,
249 2014). The best-fit parameters for each earthquake are detailed in Table S1.
250 Observed waveforms and best-fit synthetics are shown in Figures S2–S4.

251 Fifty seismograms with the best azimuthal distribution were selected, us-
252 ing data available from the Incorporated Research Institutions for Seismology
253 Data Management Center (IRIS DMC). We invert a section of the waveform
254 starting from the initial onset of the direct arrival (manually picked from
255 broadband data), and encompassing the direct arrival (P , S) and principal
256 depth phases (pP , sP , sS). The inversion window for P -waves was limited to
257 exclude subsequent water multiples, and for S -waves was limited to exclude
258 any predicted interaction with SKS arrivals. Waveforms were weighted in
259 the inversion based on azimuthal density, and S -waveforms were manually
260 weighted down by a factor of 0.5 to compensate for their increased amplitude
261 relative to the P -wave.

262 Each earthquake source was parametrised as a finite-duration rupture of
263 a point source, constrained to be a double-couple. The source duration was
264 parametrised as four 1-second elements with independent amplitudes. No
265 improvement in waveform fit was achieved when a longer duration source
266 was tested, and in many cases the final element of the allowed source time
267 function has near-zero amplitude. Hence, for each earthquake we invert
268 for nine parameters: strike, dip, rake, centroid depth, moment, and a four-
269 element source time function.

270 We use a near-source velocity structure based on the local model derived
271 from a seismic refraction experiment carried out in 2016 in the 13°N area,
272 averaged into a simple half-space (Simão et al., 2016). A water layer is added
273 over the solid Earth structure, with initial thickness from local bathymetry
274 shown in Figure 1. Small adjustments to the water layer thickness are then
275 made to best match the mean periodicity of observed P -wave water multiples.
276 In common with previous work at mid-ocean ridges we find that the inclusion
277 of a Moho, and the transition to faster mantle velocities below it, improves

278 the waveform fit for solutions with sub-Moho depths (Huang et al., 1986;
279 Jemsek et al., 1986; Huang and Solomon, 1987). This approach, however,
280 fails to produce solutions that fit better than those located above the Moho,
281 i.e. within the crust, and we hence present results using the simple half-space
282 model. Routine values of 1 and 4 s (for P - and SH -waves, respectively) are
283 used for the attenuation parameter t^* (Futterman, 1962).

284 Best-fit solutions are plotted in Figure 1a, and detailed in Table 1 and
285 Figures S2–S4. Sensitivity tests for depth and dip were performed by fixing
286 the given parameters, and inverting for the best-fit solution. When testing
287 for depth sensitivity, only centroid depth is fixed while all other parameters
288 are free to vary. When testing for dip sensitivity, dip is fixed, centroid depth
289 is fixed at the overall best-fit value, while all other parameters are free to
290 vary. For sensitivity to dip, two minima occur due to the inherent inability to
291 distinguish between the actual fault plane and the conjugate auxiliary plane
292 in the focal mechanism (Figures 4, 5, and 6).

293 Centroid depths of all three earthquakes are determined to be within
294 the upper oceanic lithosphere, at depths of < 5 km bsf (Figures 4, 5, 6,
295 and Figures S2–S4). Forcing the source depth to be > 5 km leads to pro-
296 gressively worse fits to the combined P - and SH -wave dataset (Figures 4c
297 and 5c). At depths beyond 12 km (2008 mainshock) and 18 km (2016), an
298 east/west-striking thrust-faulting mechanism appears to yield a better fit to
299 the observed waveforms than a north/south-striking normal-faulting mech-
300 anism (red points, Figures 4a and 5a). This thrust faulting mechanism is
301 an artefact of the ability to produce a reduced misfit by fitting the higher
302 amplitude part of the waveform at a subset of stations, whilst minimising the
303 amplitude at others. Although this solution may yield a marginally better
304 overall waveform misfit than a deep normal-faulting mechanism, it fails to fit
305 any identifiable first motion polarities, and cannot produce an acceptable fit
306 to the complete set of waveforms compared to a normal-faulting earthquake
307 at shallow depths.

308 Whilst an increased depth can be partially offset by reducing the source
309 duration for an individual phase, the variation in depth-phase delays at dif-
310 ferent wavespeeds (and subsequent impact on phase overlap) results in a

311 different amplitude dependence for the two phases. This trade-off is shown
312 in Figures 4b and 5b, which show that although the best-fit model is often
313 able to fit the amplitude of P -wave train at moderate depths (~ 7 km bsf), it
314 then significantly under-predicts the amplitude of the observed S -waveform.
315 This shortcoming can be partly overcome by adjusting the elastic parame-
316 ters used in the inversion, but this results in unrealistic phase separation.
317 Realistic variations in wavespeeds and near-source density produce only 1–2
318 km variation in global minimum-misfit depth. We therefore conclude that
319 only a shallow source depth is able to fit the amplitudes of both phases
320 simultaneously.

321 Absolute minimum misfit centroids for all three earthquakes occur at 2–
322 3 km bsf, indicating that rupture likely extended from near the seafloor to
323 depths of ~ 4 – 6 km bsf, assuming that earthquakes of this magnitude likely
324 rupture up to (or close to) the seafloor.

325 Best-fit focal mechanisms for all three earthquakes show north-south
326 striking normal faulting (consistent with routine catalogue results for low-
327 frequency moment tensors), with slip vectors parallel to the regional spread-
328 ing direction ($\sim 110^\circ$). Source dip resolution is hampered by the lack of
329 along-strike SH -wave data. The best-fit mechanism is achieved, however,
330 with an east-dipping planar dip of 45° for the 2016 event and a similar
331 value of 52° for the 2008 mainshock (Figure 2b). The large uncertainty in
332 dip may also reflect the depth-variable dip of the curved detachment fault
333 surface (Figures 2b and Figure 3b). The best-fit point-source solution would
334 therefore represent a moment-weighted average of the fault failure surface,
335 and values of ~ 45 – 50° would hence be consistent with peak slip at this value
336 in the centre of the rupture patch. Failure would be expected over a range of
337 dip angles either side of this central value, consistent with failure extending
338 from the downdip limit of ~ 60 – 65° to the updip limit of ~ 30 – 35° .

339 The point-source approach used here assumes that the causative fault is
340 planar. However, if the source fault is indeed the detachment, then the rup-
341 ture patch is instead likely to be curved, hence this assumption represents
342 a simplification. However, synthetic waveform tests indicate that moderate
343 down-dip curvature makes little difference to the far-field teleseismic wave-

344 forms when compared to a planar-fault model (Braunmiller and Nábělek,
345 1996). Detection of fault curvature requires both a larger-magnitude earth-
346 quake ($> M_w$ 6) and a larger rupture dimension/rupture depth range than
347 those near $13^\circ 20'N$, to allow the resolution of discrete source orientations
348 within the overall waveform, and also excellent along-strike *SH*-wave cover-
349 age. For earthquakes at the Mid-Atlantic Ridge where along-strike coverage
350 is sparse, data are limited to ocean islands, the Atlantic coast of Brazil, and
351 Iceland. While we cannot obtain evidence of down-dip curvature from the
352 waveform data, undetectable curvature of the source fault cannot be ruled
353 out.

354 Waveform inversion also yields an estimate of the shape and, of partic-
355 ular interest here, the duration of the source-time function. The estimated
356 duration trades off significantly with depth (see Figures 4 and 5). However,
357 for both the 2016 event and the 2008 mainshock, the estimated duration for
358 the best-fit model is under 4 s, with the vast majority of the moment release
359 taking place during a 2 s window. As increasing the source depth only serves
360 to shorten the estimated source duration, these estimates represent maxi-
361 mum durations for these events. Rupture propagation speeds for dip-slip
362 earthquakes rarely exceed the local shear-wave speed. Assuming an upper
363 limit on the rupture velocity of 3 km s^{-1} , the maximum dimension of the
364 main slip patch is unlikely to exceed 6 km in any direction. The short rup-
365 ture duration prevents any robust assessment of the rupture direction based
366 on waveform directivity, and hence leaves the orientation of this maximum
367 dimension undetermined.

368 **5 Large earthquakes and the $13^\circ 20'N$ OCC**

369 Slip vectors for the 2008 mainshock and 2016 earthquake (shown on Fig-
370 ure 1b) match to within 5° with the slip azimuth of the exposed fault sur-
371 face of the OCC, inferred from the trend of surface corrugations (MacLeod
372 et al., 2009; Escartín et al., 2017). A source mechanism and depth matching
373 those derived from microearthquakes cannot adequately match the observed
374 teleseismic waveforms (Figure 4b, 5b), indicating conclusively that the mi-

375 croseismicity and teleseismic earthquakes are not co-located (Parnell-Turner
376 et al., 2017). We conclude that the depth and source mechanism for these
377 earthquakes is consistent with the failure of the upper crustal section of
378 the detachment fault between the seafloor and the top of the observed mi-
379 croseismicity (7 km bsf), at moderate dip angles intermediate between the
380 steeply-dipping microseismicity ($\sim 72^\circ$) and the observed dip of the surface
381 of the exposed fault (14-18°).

382 At the TAG detachment, shallow seismicity in the footwall (<5 km bsf)
383 has been interpreted as antithetic normal faulting (deMartin et al., 2007).
384 At 13°20'N, no such faults are evident in microbathymetry of the exposed
385 fault surface (Figure 1b), nor in the microearthquake catalogue (Parnell-
386 Turner et al., 2017). The distribution of compressional seismicity within the
387 footwall indicates that any bending-related extension in the upper portion
388 of the footwall is probably limited to depths < 2 km below the detachment
389 surface, consistent with the bending of a plate with elastic-plastic rheology
390 (Parnell-Turner et al., 2017). If the M_w 5.7 event was caused by a bending-
391 related extensional fault within the top 2 km of the footwall block, then either
392 the fault must be very long in the along-strike direction, or stress drop must
393 be very high, in order to generate the necessary seismic moment. Given that
394 slip on such faults must gradually decrease to zero as the fault approaches
395 the depth of the neutral surface (2 km), the slip gradient required between
396 2 km and the surface would therefore be extremely high, and we deem this
397 explanation to be improbable.

398 Similar arguments apply to the hypothesis that these larger earthquakes
399 result from seismicity within rider blocks that could exist to the east of the
400 breakaway above the footwall. Multibeam bathymetric data show that any
401 rider blocks are restricted to the western part of the 13°20'N OCC near the
402 breakaway (Escartín et al., 2017), and are not on the multiple-km length scale
403 that would be required for fault-surfaces to host M_w 5.7 earthquakes without
404 extremely high stress drops. These rider blocks are presumably composed of
405 less coherent hanging wall material which has been subjected to extensive
406 mass wasting, and hence are unlikely to produce major earthquakes.

407 Two sub-parallel NNE-SSW trending faults, 3 km apart, can be identi-

408 fied in bathymetric data north of the 13°20'N OCC, near 13°25'N, 44°55'W
409 (Figure 1). These faults, which are ~10 km in length and appear to extend
410 from the western end of the OCC at 13°20'N to the probably inactive OCC
411 at 13°30'N, could potentially generate earthquakes with a rupture dimension
412 on order ~5 km. The dip of the exposed scarps is 40-50°, which is com-
413 patible with the nodal plane dips for the larger earthquakes, assuming these
414 faults are planar. Deep-tow sidescan sonar data show that these scarps have
415 low-amplitude backscatter, suggesting that they are not smooth exposures
416 of pristine footwall, and instead are covered in mass-wasted material or sedi-
417 ment (MacLeod et al., 2009). This overlying talus would have decreased the
418 dip angle from the true value of the fault at depth, hence these faults may
419 be steeper at depth than they appear on the seabed. These two small faults
420 were within the 2014 OBS network, which failed to detect any clustered mi-
421 croseismicity to indicate these faults are active. Whilst the same is true of the
422 shallow portion of the detachment fault, we would expect to see some degree
423 of microearthquake activity on the areas of the fault surrounding any patch
424 that ruptured in 2008 if one of these faults had hosted a larger earthquake.

425 The only other major tectonic feature within the axial valley evident in
426 bathymetric data is the eastern rift border fault (Figure 1a). Placing both
427 the 2016 event and the 2008 mainshock on this feature would require an
428 eastward shift of > 10 km from their globally constrained best-fitting loca-
429 tions. This magnitude of shift is at the limit of both the quantitative cata-
430 logue location uncertainty for these earthquakes [NEIC], and typical error in
431 global earthquake location (Lohman and Simons, 2005; Weston et al., 2012).
432 Whilst we cannot completely rule out this scenario, there is no evidence for
433 systematic westward-bias in the catalogue locations along this section of the
434 Mid-Atlantic Ridge to justify a common shift in both earthquake locations.

435 **6 Shallow detachment fault seismogenesis**

436 These results lead us to suggest that the 2008 mainshock and 2016 earthquake
437 most likely occurred on adjoining sections of the detachment fault at 13°20'N.
438 The centroid depth and overall mechanism suggest that they ruptured a

439 substantial area of the shallow part of the fault, extending from the near-
440 surface emergence of the fault, down to the presumed limit of the established
441 and contiguous fault plane, constrained by microearthquakes where the fault
442 roots near the brittle-ductile transition.

443 Using the available constraints on the geometry of the detachment fault,
444 and assuming that the 2016 earthquake and 2008 mainshock did indeed occur
445 on the detachment surface, we can estimate the minimum stress drop for the
446 2008 mainshock and 2016 earthquake. The maximum area of the detachment
447 fault that can have failed in these two earthquakes is assumed to extend from
448 the seafloor to the upper portion of the detachment-related microseismicity in
449 the down dip direction (0–7 km), and the spreading axis-parallel length over
450 which microearthquakes are observed (~ 15 km). Over the downdip extent
451 of the fault, we assume uniform curvature from 30 to 70°. We increase the
452 estimated fault area by 5% to account for the rugosity of the fault plane,
453 based on the three-dimensional surface area calculated for a 2×2 km patch
454 of the exposed fault plane using 2m-resolution microbathymetry (Escartín
455 et al., 2017). Hence our estimated total fault area is 1.3×10^8 m².

456 Since the total along-axis extent of the detachment fault exceeds the sum
457 of our estimated maximum rupture dimensions for the 2008 mainshock and
458 the 2016 earthquake, we assume that each earthquake ruptured approxi-
459 mately half of the total fault surface available on the 13°20'N detachment
460 (based on their similar magnitudes). We then estimate a minimum stress
461 drop, $\Delta\sigma$, for each earthquake by assuming $\Delta\sigma = cM_0/(A^{(3/2)})$, where A is
462 the fault area, M_0 is the moment, and c is a geometrical constant, approx-
463 imately equal to 1. We therefore determine that $\Delta\sigma \geq 0.68$ MPa for the
464 2008 mainshock, and $\Delta\sigma \geq 0.88$ MPa for the 2016 event. These stress drops
465 represent upper bounds, since decreasing the rupture area would increase the
466 stress drop in each earthquake. Nonetheless, these values are consistent with
467 stress drops observed in earthquakes in range of a tectonic regimes (Allmann
468 and Shearer, 2009), and suggest that the detachment fault is capable of sus-
469 taining significant shear stresses throughout the upper crust, down to 6 km
470 bsf. Hence this detachment fault appears to be rheologically comparable to
471 globally observed normal-fault systems in non-detachment settings.

472 It is useful to compare the results presented here with the well-studied
473 system of detachment faults at the western end of the Woodlark Basin, south-
474 eastern Papua New Guinea, which is thought to mark the transition from
475 continental extension to oceanic spreading (Little et al., 2007; Wallace et al.,
476 2014). This region contains several active detachment faults and associ-
477 ated core complexes, including the type-examples of the sub-aerial Dayman
478 Dome, and the sub-marine Moresby Seamount detachment (Spencer, 2010;
479 Speckbacher et al., 2011). Crucially, these faults have been shown to host
480 large-magnitude ($>M$ 6.0), shallowly-dipping normal-faulting earthquakes at
481 shallow depth (Abers, 1991; Abers et al., 1997). Although these detachments
482 are exhuming high-pressure metamorphic rocks in their footwalls, rather than
483 newly-formed igneous oceanic crust, the detachment-faulting process has
484 been suggested to be common to both regimes (e.g. Abers et al., 1997; Little
485 et al., 2007). Despite the presence of large-scale seismicity, recent geodetic
486 work has suggested that much of the slip on these faults is accommodated
487 aseismically through stable sliding on unlocked faults (Wallace et al., 2014),
488 although we note that the proposed coupling models did require locked faults
489 at shallow depth. In common with observations from oceanic detachment sys-
490 tems, these faults are characterised by coincident mylonitization, alteration
491 to phyllosilicate minerals, and widespread precipitation of hydrothermal cal-
492 cite and quartz, based on in samples dredged from the Moresby Seamount
493 detachment fault (Speckbacher et al., 2011).

494 Lower-crustal gabbros and mantle peridotites exposed on oceanic detach-
495 ment footwalls are commonly altered to sheet silicates such as talc and chlo-
496 rite due to pervasive hydrous circulation (e.g. Dick, 1989; Blackman et al.,
497 2002; Escartín et al., 2003; Karson et al., 2006; Blackman et al., 2014). The
498 presence of these low-friction minerals suggests that within the shallow crust,
499 slip may occur through aseismic creep along a rheologically weak fault sur-
500 face, implying that the shallow portion of a detachment fault would be unable
501 to support the stresses necessary to produce earthquakes (Escartín et al.,
502 1997; deMartin et al., 2007). In contrast, in-situ sampling of the corrugated
503 dome at $13^{\circ}20'N$ shows that, although heavily-altered ultrabasic rocks and
504 talc are present, the exposed fault surface predominantly consists of quartz-

505 cemented cataclastic metadiabase (Bonnemains et al., 2017). These rocks
506 are probably sourced from the hanging wall and later incorporated into the
507 fault zone within the uppermost few kilometres of the crust (Bonnemains
508 et al., 2017). Whilst this zone is unlikely to account for the full rupture
509 area of the larger earthquakes studied here, the migration of rupture into a
510 hanging wall comprised of quartz-cemented breccia suggests that the fault
511 surface must be at least as strong as this material. Hence the fault rheology,
512 even at shallow depths, is not dominated by minerals with low coefficients of
513 static friction—consistent with the presence of shear stresses large enough to
514 produce large earthquakes.

515 The rheological behaviour of the materials most likely to dominate the
516 fault zone (gabbroic rocks and hydrous alteration products) is highly temper-
517 ature dependent (e.g. Chernak and Hirth, 2010; Moore and Lockner, 2011).
518 A combination of variable fault rock composition and rheology, the complex
519 thermal structure at the spreading axis, and the unquantified influence of
520 variable pore fluid pressure, fault zone rheology remains highly uncertain.
521 The ability to generate large earthquakes within the uppermost few kilo-
522 metres of the fault, however, requires that the overall fault rheology in this
523 region be velocity-weakening. It remains unclear why the presence of weak
524 hydrous minerals does not appear to have inhibited seismogenic failure, or
525 had a major weakening effect on the fault itself, at least on the timescale of
526 the earthquake cycle.

527 At 13°20'N, the apparent occurrence of large-magnitude earthquakes on
528 the shallow part of the detachment fault contrasts with the microseismicity
529 that characterises the deeper, steeper-dipping sections (Figure 7), and raises
530 questions about what controls the transition in seismogenic character over
531 seemingly short length scales at depth. One important factor is likely to be
532 the thermal profile within the fault zone. However, the thermal structure
533 of oceanic detachment fault systems is difficult to ascertain with any accu-
534 racy, as a result of the complex interplay between magmatic processes, the
535 formation of new oceanic lithosphere, and widespread hydrothermal perco-
536 lation, controlled by the local permeability structure. The thermal structure
537 is intrinsically linked to the rheological evolution of the fault zone material,

538 which controls on the capacity of the fault zone to sustain stresses. The evo-
539 lution of the fault itself as the footwall is exhumed may also play a role, since
540 the active fault is thought to emerge from a ductile mylonitic shear zone at
541 depth (Hansen et al., 2013). The fault may develop as strain is localized on
542 many small brittle cracks at intermediate depths, forming as a finite-thickness
543 layer with an anastomosing fabric while generating microearthquakes (Kar-
544 son et al., 2006; Bonnemains et al., 2017), before coalescing into a single
545 coherent fault zone nearer to the surface. The transition between failure in
546 many microearthquakes to failure in large earthquakes at ~ 5 km bsf may
547 therefore represent the point at which microcracks coalesce, thus establish-
548 ing a continuous fault plane, and allowing rupture to propagate continuously
549 over large areas.

550 Earlier studies of large earthquakes at slow-spreading ridges have shown
551 that teleseismically-detected earthquakes commonly occur with centroid depths
552 of < 4 km bsf and at dip angles of 45° , within the uppermost oceanic litho-
553 sphere (Huang et al., 1986; Jemsek et al., 1986; Huang and Solomon, 1987).
554 Supra-source water depths from P -wave multiples indicate that majority of
555 these larger earthquakes occurred beneath the axial valley, potentially con-
556 sistent with their occurrence on the down-dip section of detachment faults.
557 However, lacking the bathymetric and microearthquake data to identify ac-
558 tive detachment faulting, these poorly-understood events had been assumed
559 to represent slip on rift-bounding border faults. The similarity in dip and
560 depth to the teleseismically-detected earthquakes at $13^\circ 20'N$ suggests that
561 this may not be the case, and instead, slip on the shallow portion of de-
562 tachment faults may be responsible for many more large earthquakes than
563 previously recognised. This inference is consistent with increased rates of
564 seismic moment release at detachment-dominated spreading segments, and
565 with increased estimated for the thickness of the coupled seismogenic layer
566 (Escartín et al., 2008; Olive and Escartín, 2016).

567 **7 Conclusions**

568 We find that large earthquakes at 13°20'N on the MAR are best explained
569 by rupture on the shallow, gently-dipping portion of a detachment fault. At
570 depths of ~ 10 km bsf, where the fault is presumed to initiate, a network
571 of local fractures give rise to small magnitude microearthquakes which are
572 undetected by the global teleseismic network. At shallower depths, these
573 smaller rupture patches coalesce into a coherent fault plane, strong enough to
574 produce large earthquakes which rupture substantial portions of the shallow
575 fault surface. Despite the presence of weak minerals and a transition to
576 dip-angles usually thought to be too low to support seismogenic failure, our
577 results show that oceanic detachment faults may be strong, and generate
578 earthquakes in the uppermost ~ 7 km of the lithosphere, in common with
579 those found on the continents.

580 **Acknowledgements**

581 TJC thanks the Royal Commission for the Exhibition of 1851 for financial
582 support through a Research Fellowship; RPT was supported by NSF grant
583 OCE-1458084. Several figures were produced using the Generic Mapping
584 Tools software package. Seismic data were retrieved from the IRIS Data
585 Management Center. We thank Rob Sohn and Javier Escartín for their
586 comments on a draft manuscript, and we thank the editor and two anonymous
587 reviewers for their comments.

588 **References**

- 589 G.A. Abers. Possible seismogenic shallow-dipping normal faults in the
590 Woodlark-D'Entrecasteaux extensional province, Papua New Guinea. *Ge-*
591 *ology*, 19, 1991.
- 592 G.A. Abers, C.Z. Mutter, and J. Fang. Shallow dips of normal faults dur-
593 ing rapid extension: Earthquakes in the Woodlark-D'Entrecasteaux rift
594 system, Papua New Guinea. *Journal of Geophysical Research*, 102:15301–
595 15317, 1997.
- 596 B.P. Allmann and P.M. Shearer. Global variations of stress drop for moderate
597 to large earthquakes. *Journal of Geophysical Research*, 114, 2009. doi:
598 10.1020/2008JB005821.
- 599 D K Blackman, J P Canales, and A. J. Harding. Geophysical signatures
600 of oceanic core complexes. *Geophys. J. Int.*, 178(2):593–613, 2009. doi:
601 10.1111/j.1365-246X.2009.04184.x.
- 602 D.K. Blackman, J.A. Karson, D.S. Shelly, J.R. Cann, G.L. Früh-Green, J. S.
603 Gee, S.D. Hurst, B.E. John, J. Morgan, S.L. Nooner, D.K. Ross, T.J.
604 Schroeder, and E.A. Williams. Geology of the Atlantis Massif (Mid-
605 Atlantic Ridge, 30°N): Implications for the evolution of an ultramafic
606 oceanic core complex. *Marine Geophysical Researches*, 23:443–469, 2002.
- 607 D.K. Blackman, A. Slagle, G. Guerin, and A. Harding. Geophysi-
608 cal signatures of past and present hydration within a young oceanic
609 core complex. *Geophysical Research Letters*, 41:1179–1186, 2014. doi:
610 10.1002/2013GL058111.
- 611 B. Bonnemains, J. Escartín, C. Mével, M. Andreani, and A. Verlaquet. Perva-
612 sive silicification and hangingwall overplating along the 13°20'N oceanic de-
613 tachment fault (Mid-Atlantic Ridge). *Geochemistry, Geophysics, Geosys-*
614 *tems*, 18:2028–2053, 2017. doi: 10.1002/2017GC006846.

- 615 J. Braunmiller and J. Nábělek. Geometry of continental normal faults: Seis-
616 mological constraints. *Journal of Geophysical Research*, 101:3045–3052,
617 1996.
- 618 J.R. Cann, D. K. Blackman, D.K. Smith, E. McAllister, B. Janssen, S. Mello,
619 S. Avgerinos, and E. Pascoe. Corrugated slip surfaces formed at ridge-
620 transform intersections on the Mid-Atlantic Ridge. *Nature*, 385:329–332,
621 1997.
- 622 L.J. Chernak and G. Hirth. Deformation of antigorite serpentinite at high
623 temperature and pressure. *Earth and Planetary Science Letters*, 296:23–33,
624 2010.
- 625 T. J. Craig, A. Copley, and J. Jackson. A reassessment of outer-rise seismicity
626 and its implications for the mechanics of oceanic lithosphere. *Geophysical*
627 *Journal International*, 197:63–89, 2014. doi: 10.1093/gji/ggu013.
- 628 Brian J deMartin, R. A. Sohn, J P Canales, and Susan E Humphris. Kinemat-
629 ics and geometry of active detachment faulting beneath the Trans-Atlantic
630 Geotraverse (TAG) hydrothermal field on the Mid-Atlantic Ridge. *Geology*,
631 35:711–714, 2007. doi: 10.1130/G23718A.1.
- 632 H J B Dick, M A Tivey, and B E Tucholke. Plutonic foundation of a slow-
633 spreading ridge segment: Oceanic core complex at Kane Megamullion,
634 23°30'N, 45°20'W. *Geochem. Geophys. Geosyst.*, 9(5):Q05014, 2008. doi:
635 10.1029/2007GC001645.
- 636 H.J.B. Dick. Abyssal peridotites, very slow spreading ridges and ocean ridge
637 magmatism. *Geological Society Special Publications*, 42:71–105, 1989.
- 638 J. Escartin and J P Canales. Chapman Conference on Detachments in
639 Oceanic Lithosphere: Deformation, Magmatism, Fluid Flow and Ecosys-
640 tems. *Eos Trans. AGU*, 92:31, 2011. doi: 10.1029/2011EO040003.
- 641 J. Escartín, G. Hirth, and B Evans. Effects of serpentinization on the litho-
642 spheric strength and the style of normal faulting at slow-spreading ridges.
643 *Earth Planet. Sci. Lett.*, 151(3-4):181–189, 1997.

- 644 J. Escartín, C. Mével, C.J. MacLeod, and A.M. McCaig. Constraints on
645 deformation conditions and the origin of oceanic detachments: The Mid
646 Atlantic ridge core complex at 15°45'N. *Geochemistry, Geophysics, Geosys-*
647 *tems*, 4, 2003. doi: 10.1029/2002GC000472.
- 648 J. Escartín, D.K. Smith, J. Cann, C.H. Langmuir, and S. Escrig. Central
649 role of detachment faults in accretion of slow-spreading oceanic lithosphere.
650 *Nature*, 455, 2008.
- 651 J. Escartín, C. Mével, S. Petersen, D. Bonnemains, M. Cannat, M. Andreani,
652 N. Augustin, A. Bezos, V. Chavagnac, Y. Choi, M. Godard, K. Haaga,
653 C. Hamelin, B. Ildefonse, J. Jamieson, B. John, T. Leleu, C.J. MacLeod,
654 M. Massot-Campos, P. Nomikou, J.A. Olive, M. Paquet, C. Rommevaux,
655 M. Rothenbeck, A. Steinfuhrer, M. Tominaga, L. Triebe, R. Campos,
656 N. Gracias, and R. Garcia. Tectonic structure, evolution and the nature
657 of oceanic core complexes and their detachment fault zones (13°20'N and
658 13°30'N, Mid Atlantic Ridge). *Geochemistry, Geophysics, Geosystems*, 18,
659 2017. doi: 10.1002/2016GC006775.
- 660 W.I. Futterman. Dispersive body waves. *Journal of Geophysical Research*,
661 67:5279–5291, 1962.
- 662 I. Grevemeyer, T.J. Reston, and S. Moeller. Microseismicity of the Mid-
663 Atlantic Ridge at 7°-8°15'S and at the Logatchev Massif oceanic core
664 complex at 14°40'N-14°50'N. *Geochemistry, Geophysics, Geosystems*, 14:
665 3532–3554, 2013. doi: 10.1002/ggge.20197.
- 666 L.N. Hansen, M.J. Cheadle, B.E. John, S.M. Swapp, H.J.B. Dick, B.E.
667 Tucholke, and M.A. Tivey. Mylonitic deformation at the Kane oceanic
668 core complex: Implications for the rheological behaviour of oceanic de-
669 tachment faults. *Geochemistry, Geophysics, Geosystem*, 14, 2013. doi:
670 10.1002/ggge20184.
- 671 P. Y. Huang and S. C. Solomon. Centroid Depths and Mechanisms of Mid-
672 Ocean Ridge Earthquakes in the Indian, Gulf of Aden, and Red Sea. *Jour-*
673 *nal of Geophysical Research*, 92:1361–1382, 1987.

- 674 P. Y. Huang, S.C. Solomon, E. A. Bergman, and J.L. Nabelek. Focal Depths
675 and Mechanisms of Mid-Atlantic Ridge Earthquakes from Body Waveform
676 Inversion. *Journal of Geophysical Research*, 91:579–598, 1986.
- 677 International Seismological Centre. *On-line bulletin*. Int. Seis. Cent.,
678 Thatcham, United Kingdom, 2014. <http://www.isc.ac.uk>.
- 679 J.P. Jemsek, E.A. Bergman, J.L. Nabelek, and S.C. Solomon. Focal Depths
680 and Mechanisms of Large Earthquakes on the Arctic Mid-Ocean Ridge
681 System. *Journal of Geophysical Research*, 91:13993–14005, 1986.
- 682 J.A. Karson, G.L. Fruh-Green, D.S. Kelley, E.A. Williams, D.R. Yoerger, and
683 M. Jakuba. Detachment shear zone of the Atlantis Massif core complex,
684 Mid-Atlantic Ridge, 30°N. *Geochemistry, Geophysics, Geosystems*, 7, 2006.
685 doi: 10.1029/2005GC001109.
- 686 L.S.L. Kong, S.C. Solomon, and G.M. Purdy. Microearthquake Character-
687 istics of a Mid-Ocean Ridge Along-Axis High. *Journal of Geophysical*
688 *Research*, 97:1659–1685, 1992.
- 689 T.A. Little, S.L. Baldwin, P.G. Fitzgerald, and B. Montelone. Continental
690 rifting and metamorphic core complex formation ahead of the Woodlark
691 spreading ridge, D’Entrecasteaux Islands, Papua New Guinea. *Tectonics*,
692 26, 2007. doi: 10.1029/2005TC001911.
- 693 R.B. Lohman and M. Simons. Locations of selected small earthquakes in the
694 Zagros mountains. *Geochemistry, Geophysics, Geosystems*, 6, 2005. doi:
695 10.1029/2004GC000849.
- 696 C.J. MacLeod, J. Escartín, D. Banerji, G.J. Banks, M. Gleeson, D.H.B. Irv-
697 ing, R. M. Lilly, A.M. McCaig, Y. Niu, S. Allerton, and D.K. Smith. Di-
698 rect geological evidence for oceanic detachment faulting: The Mid-Atlantic
699 Ridge, 15°45’N. *Geology*, 30:879–88, 2002.
- 700 C.J. MacLeod, R.C. Searle, B.J. Murton, J.F. Casey, C. Mallows, S.C.
701 Unsworth, K.L. Achenback, and M. Harris. Life cycle of oceanic core

- 702 complexes. *Earth and Planetary Science Letters*, 287:333–344, 2009. doi:
703 10.1016/j.epsl.2009.08.016.
- 704 C. Mallows and R.C. Searle. A geophysical study of oceanic core complexes
705 and surrounding terrain, Mid-Atlantic Ridge 13°-14°N. *Geochemistry,*
706 *Geophysics, Geosystems*, 13, 2012. doi: 10.1020/2012GC004075.
- 707 D. E. Moore and D. A. Lockner. Frictional strengths of talc-serpentine and
708 talc-quartz mixtures. *Journal of Geophysical Research*, 116, 2011. doi:
709 10.1029/2010JB007881.
- 710 A. Morris, J S Gee, N. Pressling, B. E. John, C J MacLeod, C. B. Grimes,
711 and R C Searle. Footwall rotation in an oceanic core complex quantified
712 using reoriented Integrated Ocean Drilling Program core samples. *Earth*
713 *Planet. Sci. Lett.*, 287(1-2):217–228, 2009. doi: 10.1016/j.epsl.2009.08.007.
- 714 J.-A. Olive and J. Escartín. Dependence of seismic coupling on normal fault
715 style along the Northern Mid-Atlantic Ridge. *Geochemistry, Geophysics,*
716 *Geosystems*, 17:4128–4152, 2016. doi: 10.1002/2016GC006460.
- 717 R Parnell-Turner, R. A. Sohn, C. Peirce, T J Reston, C J Macleod, R C
718 Searle, and N. M. Simão. Oceanic Detachment Faults Generate Compression
719 in Extension. *Geology*, 2017. doi: 10.1130/G39232.1.
- 720 N. Simão, C. Peirce, Matthew Falder, T J Reston, C J Macleod, and R C
721 Searle. Velocity structure of the crust at 13N on the Mid-Atlantic Ridge:
722 implications for crustal accretion and oceanic core complex formation. *Ab-*
723 *stract T33A-2997 presented at 2016 Fall Meeting, AGU, San Francisco,*
724 *Calif. 12-16 Dec, 2016.*
- 725 D.K. Smith, J.R. Cann, and J. Escartín. Widespread active detachment
726 faulting and core complex formation near 13°N on the Mid-Atlantic Ridge.
727 *Nature*, 442:440–443, 2006.
- 728 S.C. Solomon and P.Y. Huang. Centroid depths and mechanisms of mid-
729 ocean ridge earthquakes in the Indian Ocean, Gulf of Aden, and Red Sea.
730 *Journal of Geophysical Research*, 92:1361–1382, 1987.

- 731 R. Speckbacher, J.H. Behrmann, T.J. Nagel, M. Stipp, and C.W. Devey.
732 Splitting a continent: Insight from submarine high-resolution mapping of
733 the Moresby Seamount detachment, offshore Papua New Guinea. *Geology*,
734 39:651–654, 2011. doi: 10.1130/G31931.1.
- 735 J.E. Spencer. Structural analysis of three extensional detachment faults with
736 data from the 2000 Space-Shuttle Radar Topography Mission. *GSA Today*,
737 20:4–10, 2010.
- 738 L.R. Sykes. Mechanism of earthquakes and nature of faulting on the mid-
739 ocean ridges. *Journal of Geophysical Research*, 72:2131–2153, 1967.
- 740 F. J. Tilmann, T. J. Craig, I. Grevemeyer, B. Suwargadi, H. Kopp, and
741 E. Flueh. The updip seismic/aseismic transition of the Sumatra megath-
742 rust illuminated by aftershocks of the 2004 Aceh-Andaman and 2005 Nias
743 events. *Geophysical Journal International*, 181:1261–1274, 2010. doi:
744 10.1111/j.1365-246X.2010.04597.x.
- 745 D.R. Toomey, S.C. Solomon, G.M. Purdy, and M.H.H. Murray. Mi-
746 croearthquakes beneath the median valley of the Mid-Atlantic Ridge near
747 23°N: Hypocenters and focal mechanisms. *Journal of Geophysical Re-
748 search*, 90:5443–5458, 1985.
- 749 B.E. Tucholke, J. Lin, and M.C.C. Kleinrock. Megamullions and mul-
750 lion structure defining oceanic metamorphic core complexes on the Mid-
751 Atlantic Ridge. *Journal of Geophysical Research*, 103:9857–9866, 1998.
- 752 L.M. Wallace, S. Ellis, P. Tregoning, N. Palmer, R. Rosa, R. Stanaway,
753 J. Oa, E. Nidkombu, and J. Kwazi. Continental breakup and UHP rock
754 exhumation in action: GPS results from the Woodlark Rift, Papua New
755 Guinea. *Geochemistry, Geophysics, Geosystems*, 15:4267–4290, 2014. doi:
756 10.1002/2014GC005458.
- 757 J. Weston, A. G. Ferreira, and G.J. Funning. Systematic comparisons
758 of earthquake source models determined using InSAR and seismic data.
759 *Tectonophysics*, 532-535:61–81, 2012. doi: 10.1016/j.tecto.2012.02.001.

760 C.J. Wolfe, G.M. Purdy, D.R. Toomet, and S.C. Solomon. Microearthquake
761 characteristics and crustal velocity structure at 29°N on the Mid-Atlantic
762 Ridge: The architecture of a slow spreading segment. *Journal of Geophys-*
763 *ical Research*, 100:24449–24472, 1995.

764 P. Zwick, R. McCaffrey, and G. Abers. MT5 program. *IASPEI Software*
765 *Library*, 4, 1994.

Identifier	Date & Time	Depth (km bsl)	Moment (N m)	M_w	Strike ($^\circ$)	Dip ($^\circ$)	Rake ($^\circ$)
Microseismicity	-	10–14	-	-	352	72	-105
2008 Mainshock	2008/12/07 06:23:10	6.0	3.555×10^{17}	5.7	343	52	-104
2008 Aftershock	2008/12/08 01:51:01	5.0	2.663×10^{17}	5.6	350	46	-093
2016	2016/10/20 00:09:26	5.1	4.620×10^{17}	5.7	345	45	-105

Table 1: **Mechanism parameters for seismicity near 13°20’N.** Values for microseismicity are taken from Parnell-Turner et al. (2017). Values for the three larger earthquakes are based on waveform modelling (this study), shown in Figures S2–S4.

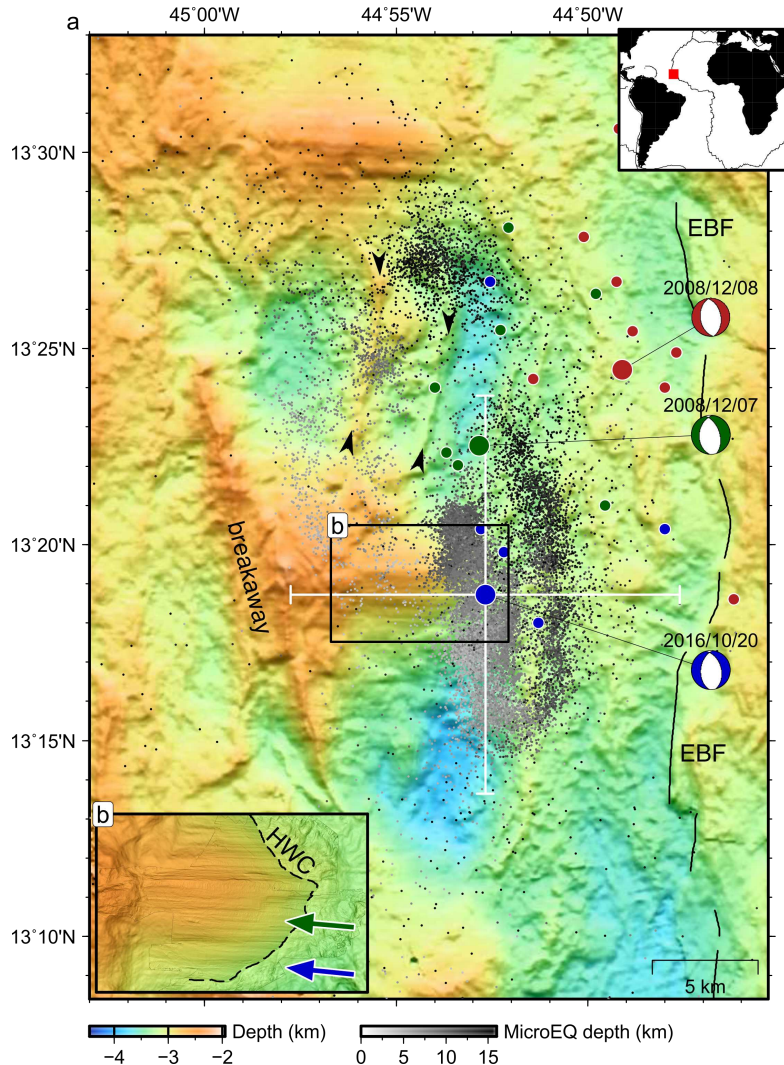


Figure 1: **Bathymetry and earthquakes.** Inset: red box shows study location. (a) Small dots are microearthquakes shaded by depth (Parnell-Turner et al., 2017); large blue circle is preferred hypocentre for M_w 5.7 event on 20th October 2016 (NEIC catalogue); large green/red circles are hypocentres for M_w 5.6/5.5 events on 7th/8th December 2008 events, respectively (ISC catalogue); focal mechanisms shown are best fitting solutions from this study; small coloured circles are unfavoured hypocentres from alternative catalogues (see Table S1 for details); solid black line is eastern border fault (EBF); arrow tips mark small fault scarps near OCC. (b) Detailed view of corrugated fault surface, with 2 m resolution microbathymetry (Escartín et al., 2017, French Oceanographic Cruises, <http://dx.doi.org/10.17600/13030070>), blue/green arrows indicate slip direction of 2016/2008 main shocks, respectively; dashed line is hanging wall cutoff (HWC).

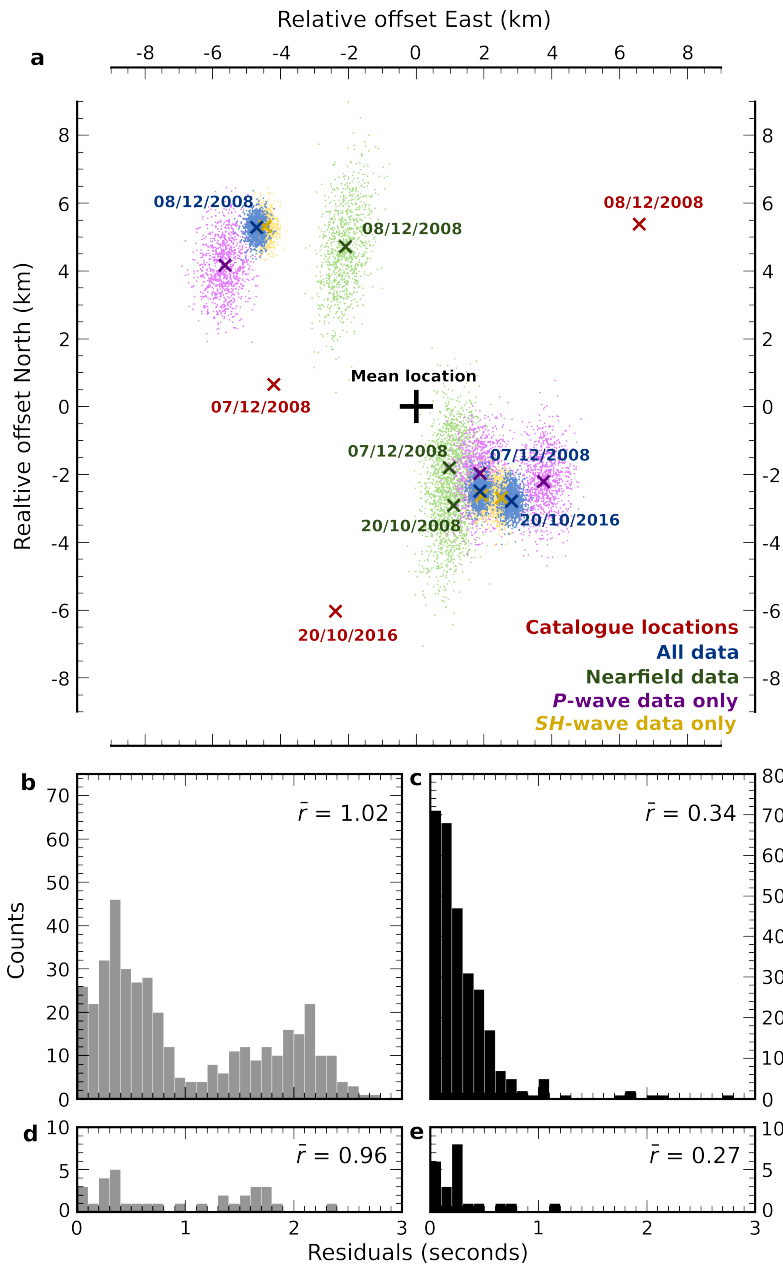


Figure 2: **Relative relocation of teleseismic earthquakes.** (a) Relative earthquake locations for the three teleseismically-observed events. Sets of locations are shown relative to their common mean, defined as plot origin, shown by large black cross. Red crosses are initial catalogue locations. Blue crosses are locations after relocation using all data. Green crosses are relocations using only data at epicentral distances $< 30^\circ$. Purple/yellow crosses are relocations using only *P*-wave/*SH*-wave data, respectively. Small coloured points show 1000 relocations after relative time dataset has been randomly perturbed based on a normal distribution of width defined by mean post-relocation residual. (b) Cross-correlation derived residuals prior to relocation for all data. \bar{r} indicates the mean residual. (c) Residuals after relocation using all data. (d),(e) as for (b),(c), but showing residuals for relocation using only data at epicentral angles $< 30^\circ$.

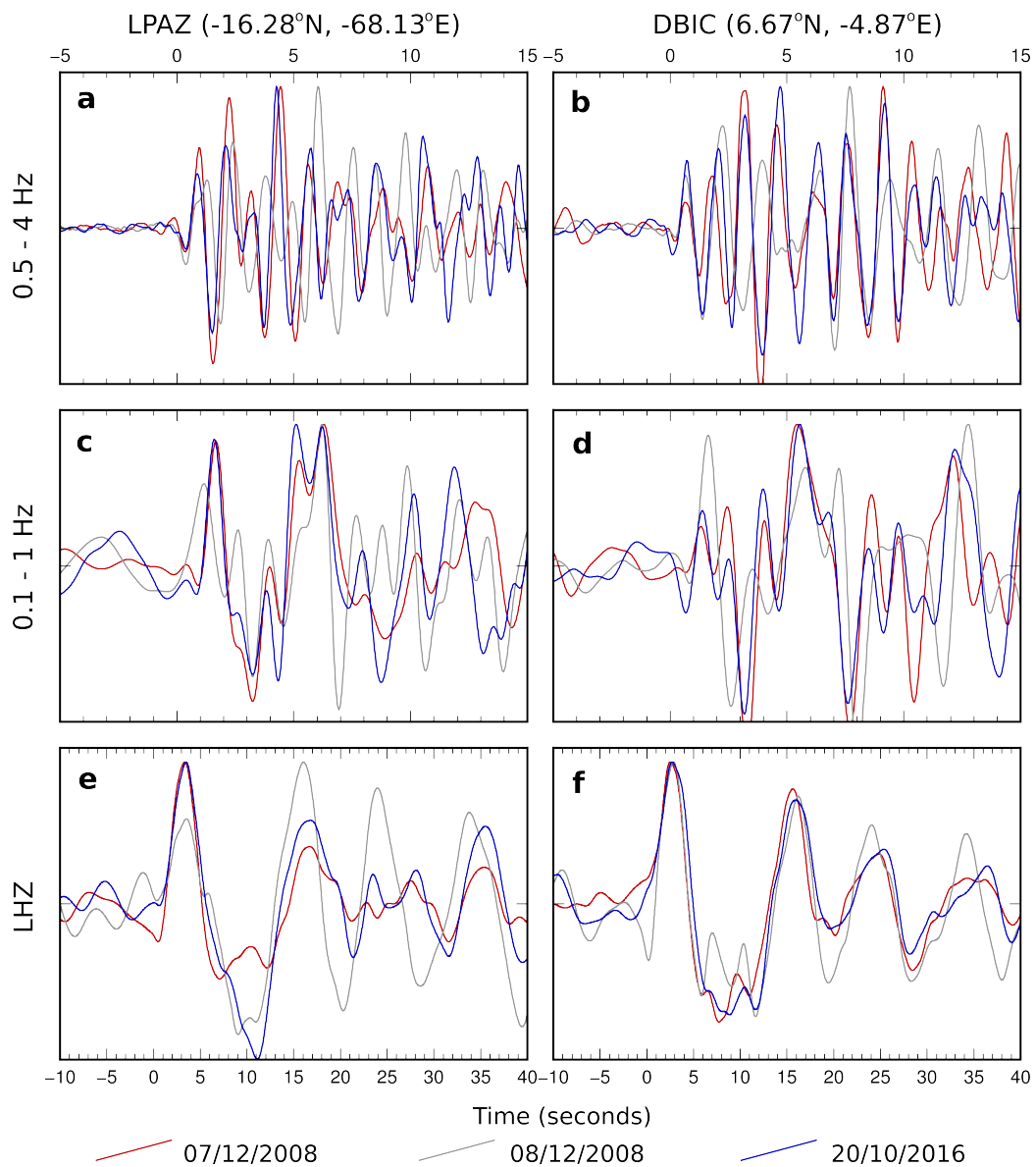


Figure 3: **Waveform comparisons at different frequency bands.** Left column shows waveforms from station LPAZ in Bolivia. Right column shows waveforms from station DBIC in Cote d'Ivoire. Waveforms aligned relative to *P*-wave arrival. (a,b) Waveforms subject to 4-pole Butterworth filter with pass band 0.5–4 Hz. (c,d) Waveforms subject to 4-pole Butterworth filter with pass band 0.1–1 Hz. (e,f) Waveforms converted to tapered frequency response of a long-period seismometer.

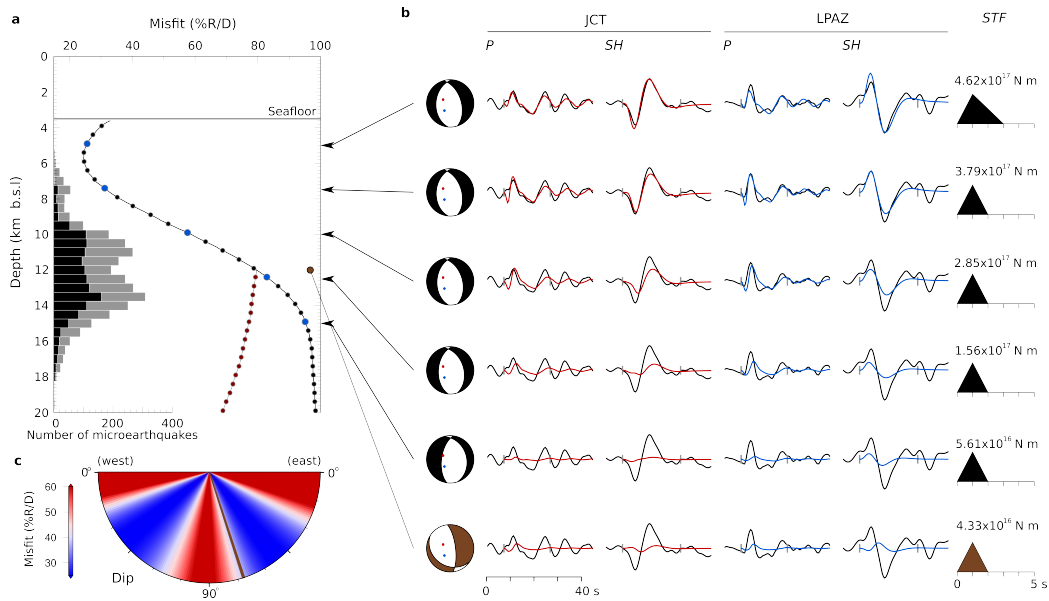


Figure 4: **Analysis of 7th December 2008 earthquake.** (a) Waveform misfit as a function of depth. Black line/points are for solutions with prior assumption of north-striking normal fault. Blue points indicate depth values used for sensitivity examples shown in b. Grey line/red points are for fully unconstrained solutions. Histograms show depth of extensional microearthquakes from Parnell-Turner et al. (2017), grey for all extensional earthquakes, black for only those adjacent to corrugated dome at 13°20'N. (b) Depth-sensitivity tests at depths of 5, 7.5, 10, 12.5, and 15 km bsl. Left column shows best-fit focal mechanism for each depth interval. Red/blue points show projection of two example stations, JCT and LPAZ, respectively. Following four columns show *P*- and *SH*-waveforms for stations JCT and LPAZ. Black traces are observed waveforms, coloured traces are synthetic waveforms for best-fit solution at each depth. Black vertical ticks indicate inversion window. Right hand column shows best-fit source-time function and moment for each depth. Bottom row shows waveforms calculated with depth and mechanism fixed to match values for microearthquake composite mechanism (Parnell-Turner et al., 2017). (c) Dip sensitivity tests. Brown bar shows dip value of composite focal mechanism for normal-faulting microseismicity at base of detachment fault (72°).

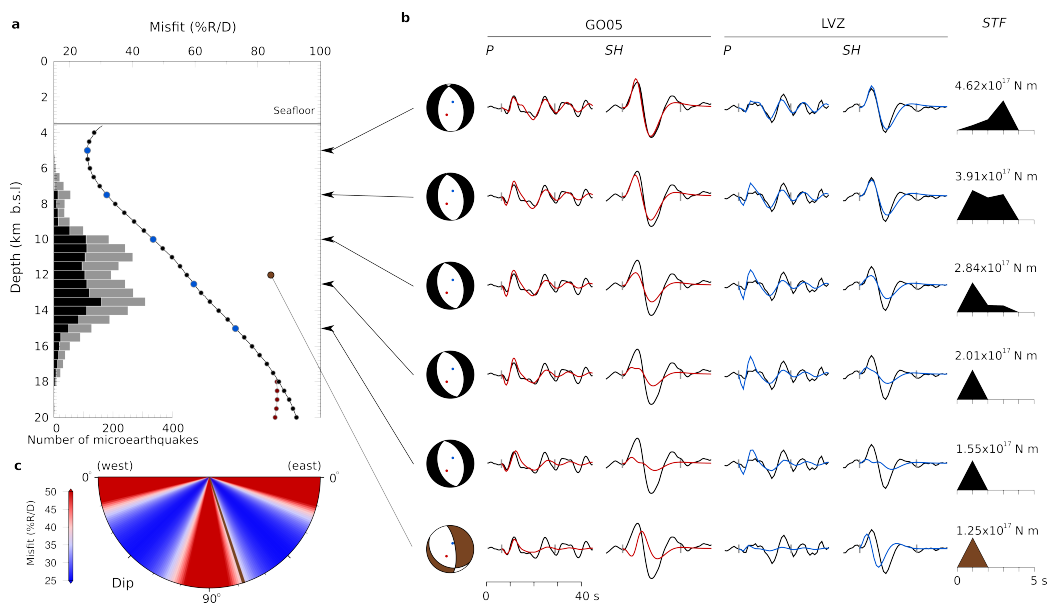


Figure 5: **Analysis of 20th October 2016 earthquake.** (a) As in Figure 4. (b) As in Figure 4, except with stations G005 and LVZ substituted for JCT and LPAZ. (c), (d) As in Figure 4.

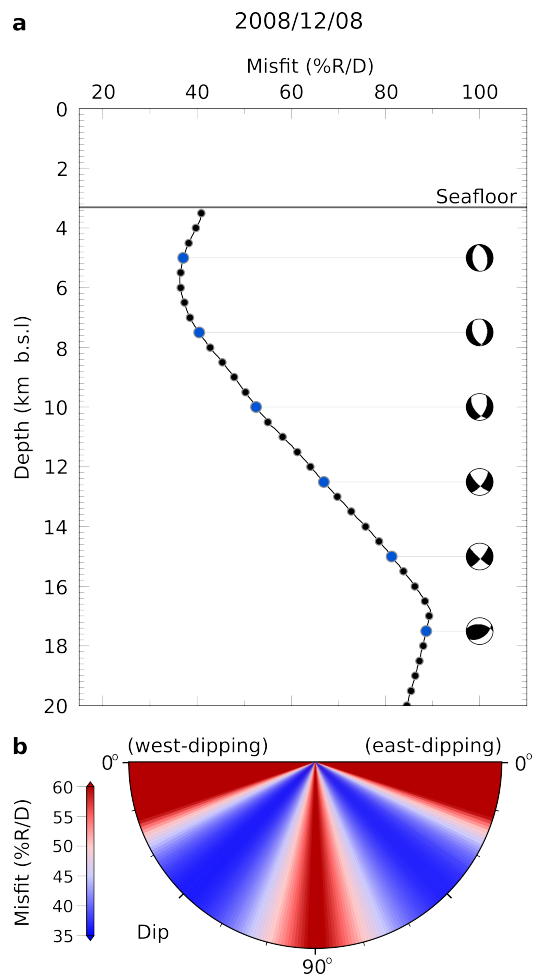


Figure 6: **Analysis of 8th December 2008 earthquake.** (a) Waveform misfit as a function of depth, calculated at 0.1 km depth intervals. At each depth, best-fit solution is calculated based on free inversion for all source parameters, except depth. Best-fit focal mechanisms shown at 2.5 km increments. (b) Dip sensitivity tests for east-most and west-most dipping planes for 8th December 2008 earthquake. At each dip-value, dip and centroid depth are fixed (at overall best-fit value for centroid depth), while all other parameters vary freely.

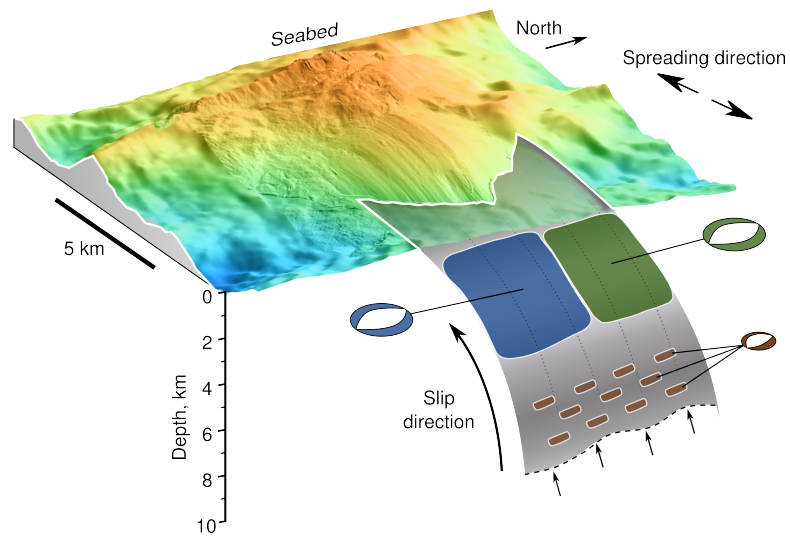


Figure 7: **Three-dimensional sketch showing bathymetry and rupture at 13°20'N detachment fault.** Grey curved area is portion of detachment fault surface; focal mechanism solutions and rupture patches for 2016 event (blue), 2008 mainshock (green) and subset of microearthquakes (brown) plotted in their expected positions on fault surface. Black arrows show spreading/slip direction. Microbathymetry from (Escartín et al., 2017, French Oceanographic Cruises, <http://dx.doi.org/10.17600/13030070>), with colour shading as in Figure 1.